

# Purely equatorial lasing in spherical liquid crystal polymer microlasers with engineered refractive index gradient

David Ripp<sup>1</sup>, Nachiket Pathak<sup>1</sup>, Vera M. Titze<sup>1,2</sup>, Andreas Mischok<sup>1</sup>, Marcel Schubert<sup>1,\*</sup>

<sup>1</sup>Humboldt Centre for Nano and Biophotonics, Department of Chemistry and Biochemistry, University of Cologne, Cologne, Germany.

<sup>2</sup>Department of Sustainable and Bio-inspired Materials, Max Planck Institute of Colloids and Interfaces, Potsdam, Germany

\*marcel.schubert@uni-koeln.de

## Abstract

Liquid crystal whispering gallery mode microlasers show high sensitivity to external stimuli and distinct spectral features, rendering them ideally suited for various sensing applications. They also offer intrinsic anisotropic optical properties, which can be used to shape and manipulate light even inside spatially highly symmetric structures. Here, we report the synthesis and detailed optical characterization of a spherical bipolar liquid crystal polymer microlaser that tightly confines the optical path of whispering gallery modes to the equatorial plane. By controlled anchoring of the liquid crystal mesogens followed by polymerization, a fixed refractive index gradient is formed within the spherical microcavity. Consequently, only transverse electric (TE) modes oscillating in the equatorial plane experience the high extraordinary refractive index, allowing to confine lasing into a single plane. Furthermore, we observe that the refractive index gradient causes a characteristic splitting of the TE modes. By combining hyperspectral imaging and analytical modeling, we demonstrate that the observed splitting is caused by lifting of the energy degeneracy of higher order azimuthal laser modes, enabling direct insights into the complex interplay of refractive index gradients and resulting whispering gallery mode confinement. In addition, the unique ability to confine lasing of a spherical microbead into only a single plane makes these microlasers independent of the exact position of the pump beam, which allows consistent localized sensing especially in combination with fast point scanning microscopes or inside highly dynamic biological environments.

## Introduction

Whispering gallery mode (WGM) microlasers have emerged as a versatile tool for a broad range of sensing applications.<sup>1,2</sup> Isotropic solid microlasers with high sensitivity to changes in the external refractive index have been widely explored for biosensing.<sup>1,3-7</sup> Through surface functionalization, solid microlasers have enabled the detection of proteins and DNA molecules<sup>8,9</sup>, while their narrow linewidth emission has been exploited for cellular tagging and tracking<sup>10,11</sup>. Liquid crystal and oil droplet WGM microlasers provide an alternative sensing platform, detecting temperature<sup>12-16</sup>, electric fields<sup>17-19</sup>, mechanical forces<sup>20,21</sup>, biochemical molecules<sup>22-24</sup>, metal ions<sup>25</sup>, and surfactants<sup>26</sup>.

Due to their high symmetry, spherical WGM microresonators can support lasing along the inner circumference formed by the intersection of any plane that contains the center of the sphere. Therefore, the exact light path of the WGMs is often not fixed and will change depending on where the microresonator is pumped, and whether there are structures close to the surface that can interact with the WGMs and potentially degrade the quality factor. This also means that WGMs can potentially reach any point on the surface of the resonator. This effect becomes apparent when employing scanned excitation schemes such as in light sheet microscopy<sup>27</sup> or confocal hyperspectral imaging<sup>28</sup>, where the WGMs change their oscillation plane depending on the exact position of the pump spot. Here, it is also observed that light incoupling is most efficient at the rim of the microlasers while no or only very weak lasing is observed when the pump laser excites the center of the microspheres<sup>27</sup>.

A possible way to manipulate the light propagation inside of optical resonators is to modify their shape or to engineer the spatial distribution of the refractive index. The former was demonstrated in oil droplets, where the deformation into ellipsoids induces symmetry breaking and mode splitting<sup>20</sup>. Manipulation based on the refractive index has most impressively been demonstrated in liquid crystal based microlasers<sup>24,26</sup> or in microbeads made from conjugated polymers with chiral morphologies.<sup>29</sup> In some cases, mode splitting into distinct modes has been reported in bipolar liquid crystal droplets<sup>26</sup>, yet without spatial localization of the individual modes within the microlaser or a detailed analysis about the origin of the splitting. Solid WGM microresonators with bipolar structures have also been demonstrated, but their photoluminescent emission spectrum lacks narrow WGM modes<sup>30,31</sup>. Moreover, spherical microlasers in which whispering

gallery mode confinement is restricted to a single plane have not been demonstrated to date. Thus, liquid crystal-based microlasers so far display the most versatile system to manipulate light propagation inside spherical microresonators. However, pure liquid crystal phases might be easily deformable or even undergo phase transitions e.g. by changes of the surrounding temperature or surface-anchoring molecules<sup>18,24-26</sup>. Furthermore, for applications in biosensing it is also important to note that their liquid crystalline nature constitutes a significant risk given the recent assessment of the high toxicity<sup>32-34</sup> of many liquid crystal monomers.

In this work, we introduce bipolar liquid crystal polymer whispering gallery mode microlasers with low lasing thresholds and purely equatorial lasing. The microlasers show orientation-dependent lasing that is sensitive to the relative orientation between the bipolar axis and the excitation beam. We further demonstrate that WGM lasing is only possible in the equatorial plane and that the corresponding lasing spectra has a distinct mode splitting. The spatial localization of these modes within the microlaser and the lifting of the mode degeneracy are explained by the refractive index gradient arising from the bipolar liquid crystal configuration within the microlaser. Our results provide a detailed understanding of the interaction of light inside non-isotropic optical resonators, while the unique lasing characteristics also provide new possibilities for localized biosensing.

## Results and Discussion

To engineer the refractive index gradient inside spherical microlasers, a liquid crystal polymer system was selected to combine anisotropic optical properties with the biocompatibility and mechanical advantages offered by a solid phase material. In this system, the molecular alignment of the mesogen-containing side chains of the polymer creates a direction-dependent refractive index, which will be the key to control light propagation in otherwise perfectly symmetric microspheres. We use rod-shaped acrylate-based monomers (Fig. 1b) and bi-acrylate crosslinkers (Fig. 1c) as the mesogens to form the liquid crystal phase, while polyvinyl alcohol (PVA) is used as a surfactant to induce planar anchoring, uniform alignment of the mesogens, and self-assembling into a bipolar configuration. A subsequent crosslinking step (Fig. 1a) then arrests the molecular orientation and creates a polymer bead with anisotropic optical properties. To achieve lasing, optical gain is introduced by adding the strongly fluorescent dye DCM (Fig. 1d) into

the mesogen mixture. With this molecular system, we aim to create liquid crystal polymer WGM microlasers where lasing is confined to only a single plane (Fig. 1e). Measurements of the refractive index (Fig. 1f) of an isotropic, non-aligned liquid crystal film yields a refractive index of 1.596 (at 600 nm), almost identical to the refractive index of isotropic polystyrene which is widely used as polymer matrix for microlasers<sup>5,10</sup>. Upon alignment and formation of a liquid crystal phase, the polymer exhibits a pronounced optical anisotropy, with the ordinary refractive index measured to be  $n_o = 1.511$  and an extraordinary refractive index of  $n_e = 1.661$  (both at 600 nm). The high extraordinary refractive index supports highly efficient confinement of light and enables WGM resonances and lasing in very small microspheres.

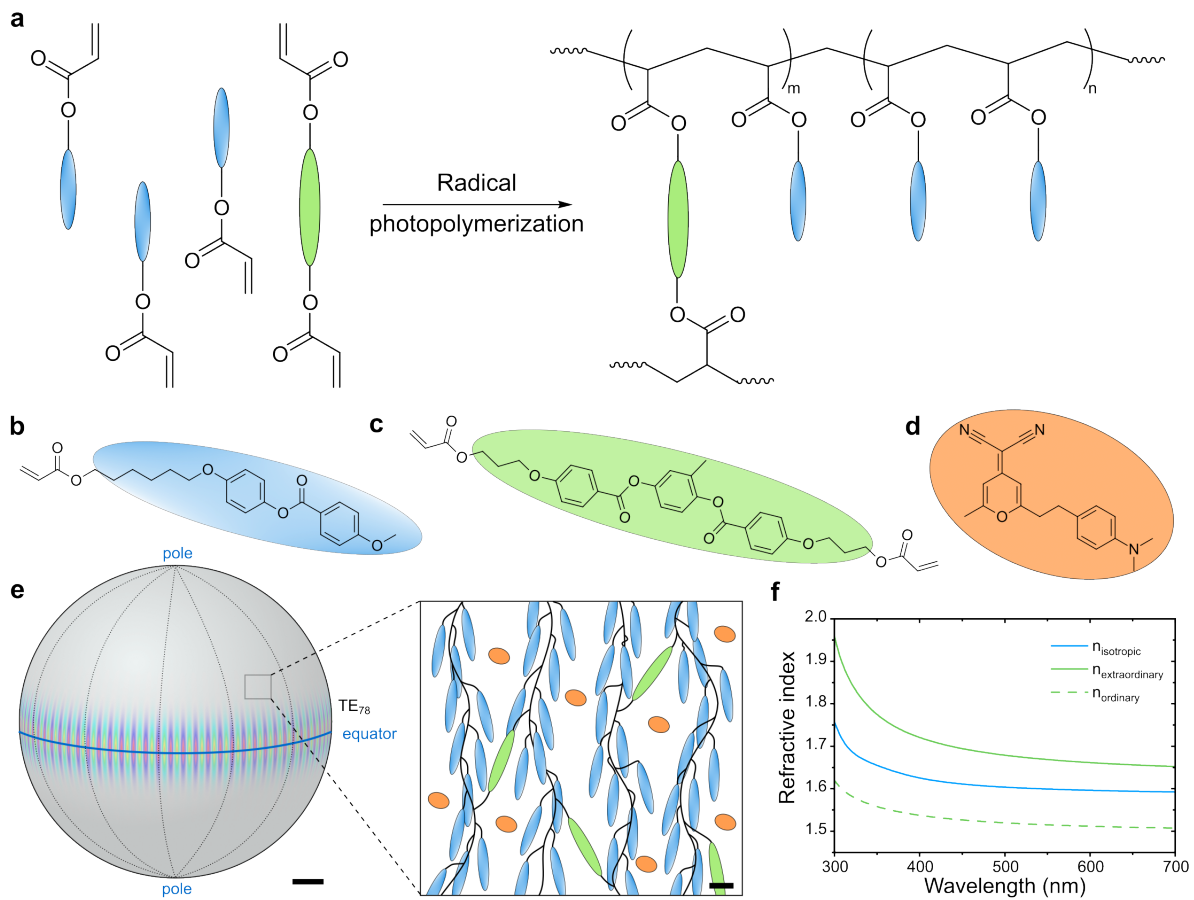


Figure 1: Schematic representation (a) of the radical photopolymerization reaction between mesogens that create the polymer backbone and crosslinks between the chains. Molecular structures of (b) the monomer (blue), and (c) the crosslinker (green) mesogens, and of (d) the lasing dye DCM (orange). (e) Schematic illustration of a 10  $\mu\text{m}$  large microlaser and a whispering gallery mode (with transverse electric (TE) polarization and an angular momentum quantum number of  $l = 78$ ) confined to the equatorial plane. Scale bar, 1  $\mu\text{m}$ . The inset shows an illustration of the molecular structure of the polymer with aligned liquid crystal side chains. Dye molecules (orange) are embedded in the liquid crystal polymer matrix to provide

optical gain. Scale bar,  $\sim 1$  nm. (f) Measured ordinary (dashed green line), extraordinary (solid green line) and isotropic (blue line) refractive index curves of the liquid crystal polymer.

Monodisperse liquid crystal polymer microlasers were prepared using a focused flow droplet generator microfluidic chip with a nozzle size of  $20\text{ }\mu\text{m}$  (Fig. 2a). Molecular alignment into a bipolar liquid crystal phase within the droplets was achieved by adding PVA as a surfactant to the continuous phase. The dispersed phase consisted of a mixture of monomer, crosslinker, initiator, and DCM dissolved in dichloromethane. In a first step, droplets with diameters of approximately  $25$  to  $30\text{ }\mu\text{m}$  were generated via pressure regulated flow of the two phases. Subsequent solvent evaporation caused the droplets to shrink into pure liquid crystal droplets with diameters of approximately  $9$  to  $10\text{ }\mu\text{m}$  (Fig. 2b). Finally, UV induced crosslinking was used to fix the molecular alignment and to create solid liquid crystal polymer microlasers.

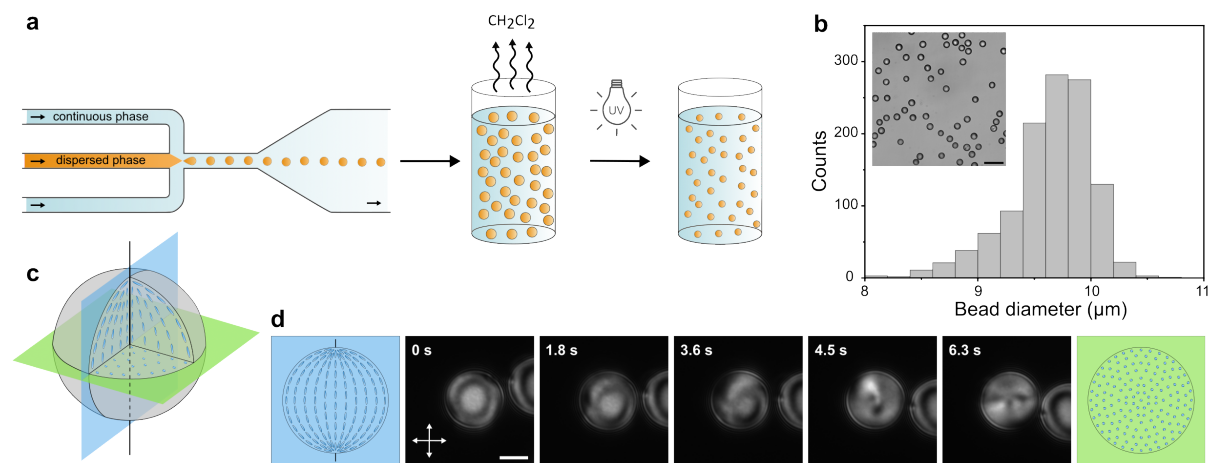


Figure 2: (a) Fabrication of liquid crystal polymer microlasers. Droplets of the dissolved mixture of the monomer, crosslinker, initiator, and lasing dye were prepared by microfluidics. The droplets were left until the solvent evaporated and subsequently polymerized by UV light to preserve the orientation of the liquid crystal molecules. (b) Typical size distribution of the resulting microlasers. Inset: Bright field microscopy image of the microlasers. Scale bar,  $25\text{ }\mu\text{m}$ . (c) Schematic representation of the bipolar orientation of the mesogens inside the microlasers. Two cross-sections are shown, one through the plane containing the poles (blue) and one through the equatorial plane (green). (d) A series of cross-polarized images of a rolling microlaser. The first and last microscopy images depict the appearance of a bipolar microlaser in cross-polarized imaging when viewed sideways onto the bipolar axis or along the bipolar axis, respectively. For both cases, the orientation of the mesogens in the image is shown schematically.

The prepared microlasers exhibit a bipolar internal structure (Fig. 1e, 2c) arising from the alignment of the mesogens. This bipolar configuration creates a refractive index gradient inside the microspheres, where the high extraordinary refractive index component is only

oriented along the lines that run from one pole to the other (meridians). The orientation of this internal structure is confirmed experimentally by the observation of characteristic optical textures in cross-polarized images of a microbead rolling from one orientation to the other, transitioning from a side view of the bipolar axis to a top view along the bipolar axis (Fig. 2d). Therefore, in cross-polarized images, a ring-like intensity distribution is observed for microlasers oriented with a side view onto the bipolar axis, whereas a cross-like or defect-like pattern is observed when the microlasers are viewed along the bipolar axis.

The high refractive index of the liquid crystal polymer enables efficient optical confinement via total internal reflection, supporting WGMs even for microspheres with diameters as small as 9 to 10  $\mu\text{m}$  that are immersed in aqueous environments. First, threshold measurements were performed to establish the typical pulse energy needed to generate WGM lasing. To avoid translational and rotational motion during the threshold measurements, microlasers were immobilized in a low concentration agarose gel. A representative input-output curve for a 9.5  $\mu\text{m}$  diameter microlaser in a sideways orientation is shown in Fig. 3a, which has a threshold energy of 85 pJ. Emission spectra below and above threshold confirm the presence of WGMs (Fig. 3b). Statistical analysis of similarly oriented microlasers reveal an average threshold of approximately 87 pJ (Fig. 3c). Also visible is a pronounced splitting of the laser modes, which creates groups of 3-5 well-resolved modes, each about 200-300 pm apart, and progressively decreasing in intensity (Fig. 3b,d).

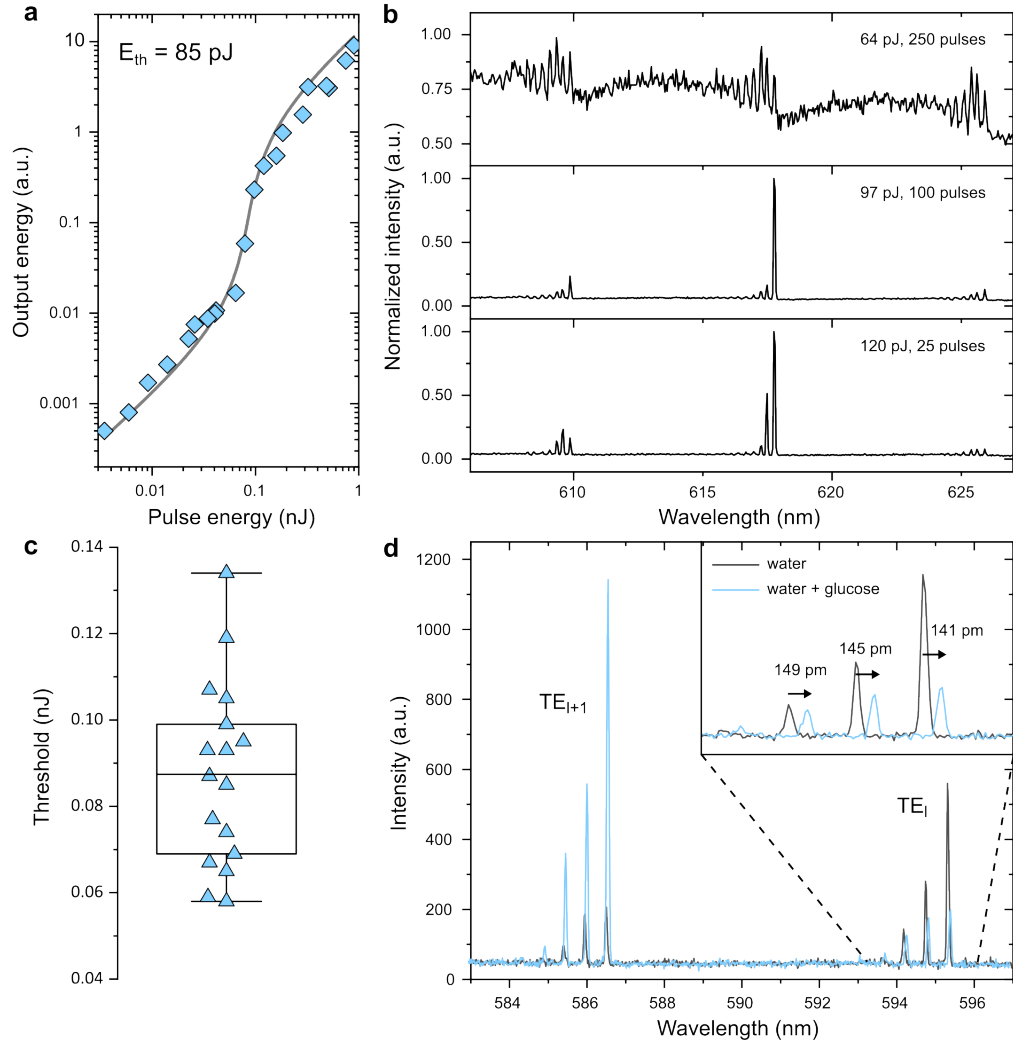


Figure 3: **(a)** Measured input-output characteristics (blue symbols) of a bipolar microlaser under pulsed excitation. Also shown is a fitted threshold curve (black line), corresponding to a threshold energy of 85 pJ. **(b)** Normalized lasing spectra at different pump energies below and above the laser threshold corresponding to the input-output curve in (a). Only modes with TE polarization as well as splitting of the modes are observed. **(c)** Distribution of measured laser thresholds of  $N=17$  microlasers with diameters ranging from 9 to 10  $\mu\text{m}$ . The box plot shows the mean and standard deviation, while whiskers represent the 5<sup>th</sup> and 95<sup>th</sup> percentile. **(d)** Lasing spectra of a single microlaser measured in two different media, showing collective red shift of the split modes in the medium with higher refractive index (water + glucose). The shift is very similar for the two observed angular momentum mode numbers ( $TE_l$  and  $TE_{l+1}$ ).

To investigate the nature of the mode splitting, a refractive index sensing experiment was performed where we tracked the shift of each observed mode of a single microlaser upon changing the external refractive index (Fig. 3d). A concentrated glucose solution was added to a known volume of an aqueous suspension of microlasers with a final glucose concentration of 3% w/v. This increased the measured refractive index of the surrounding medium from 1.333 to 1.337. As expected, a red shift of approximately 145 pm was

observed for all lasing modes. Notably, within a single split peak, sub-modes at shorter emission wavelength show a slightly larger red shift. Theoretical calculations of the WGM positions (assuming a homogeneous refractive index) predict a shift of approximately 95 pm<sup>3,35</sup>, which is in good agreement with the experimentally measured values. We attribute the difference between the experimentally measured and the calculated wavelength to inhomogeneous mixing of the glucose solution, resulting in a higher local refractive index. Because the refractive index change is sensed by the evanescent component of a WGM, the observation that all modes shift similarly implies that they are located on the microlaser surface and have a similar extend of the evanescent field as it is the case for the energetically degenerate azimuthal modes inside of spherical resonators<sup>2,20</sup>. Furthermore, the expected free spectral range ( $\lambda_{TE, I} - \lambda_{TE, I+1}$ ) for a 10  $\mu\text{m}$  large microsphere emitting around 600 nm is about 9 nm, consistent with the observed difference between the groups of modes (Fig. 3b,d). In contrast, the expected difference between TE and TM modes ( $\lambda_{TE, I} - \lambda_{TM, I}$ ) is expected to be 3.5 nm. As we do not observe modes with this spacing in any of the spectra, we conclude that in this size range and in an aqueous environment only TE but not TM modes are supported in our bipolar microlasers. We will show that this assumption is also supported by the detailed geometrical analysis of the mode polarization and molecular orientation that we describe further below.

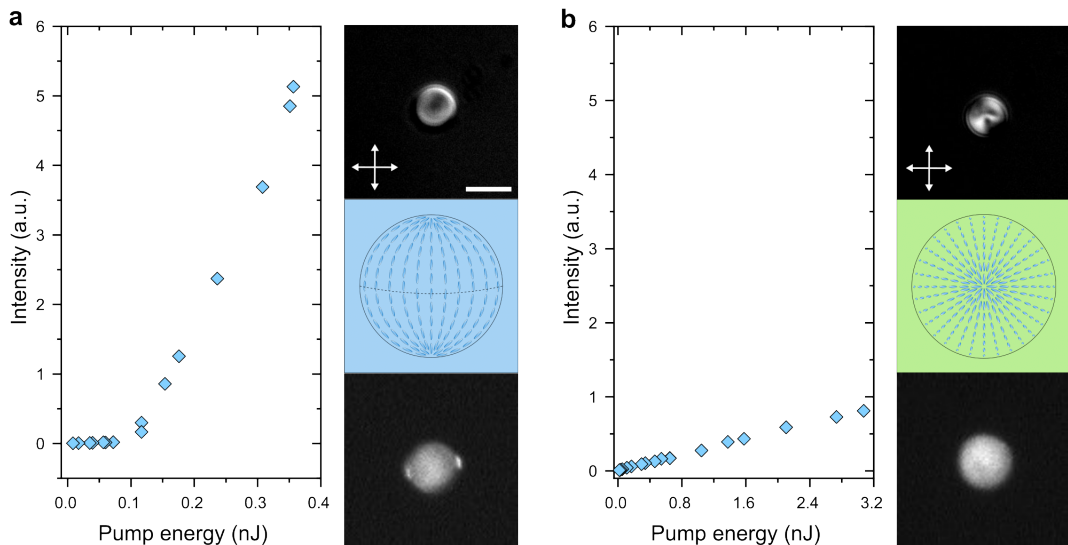
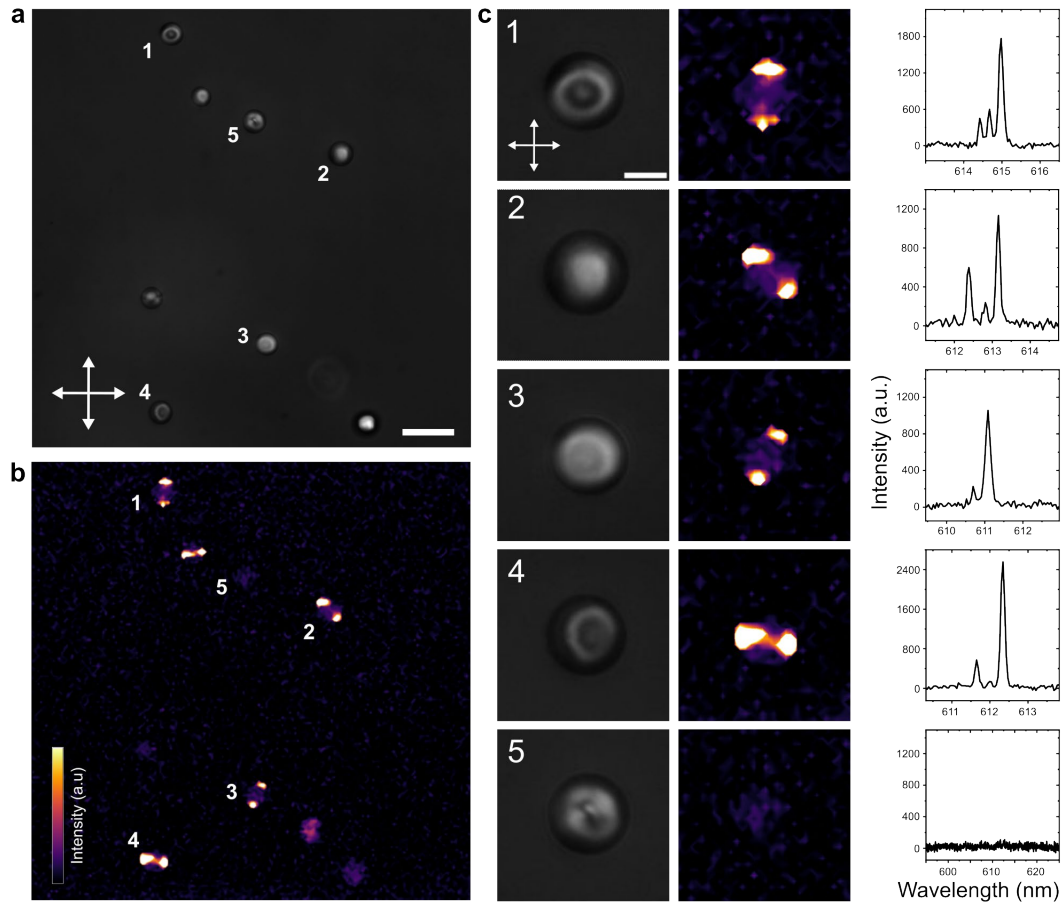


Figure 4: Threshold curves (left) and microscopy images (right) of microlasers oriented **(a)** sideways in relation to their bipolar axis, and **(b)** in a polar facing orientation. For (a) and (b), the corresponding cross-polarized images (top), schematic representation of the liquid crystal orientation in a 3D sphere (middle),

and a fluorescence microscopy image are shown. The two bright spots in (a, bottom right) indicate lasing in the equatorial plane while only homogeneous fluorescence is observed in (b, bottom right). For pumping, a large homogeneous beam with a diameter of  $\sim 45 \mu\text{m}$  was used. Scale bar,  $10 \mu\text{m}$ .

Having established the strongly anisotropic bipolar structure of the microlasers and that the spectrum only consists of TE modes, we analyzed how microlaser characteristics change with their orientation. First, we measured a microlaser lying sideways on the bipolar axis with the orientation information being inferred from the ring-like pattern in cross-polarized optical images (Fig. 4a), for which we observe a similar lasing threshold as before. In contrast, a microlaser oriented along the bipolar axis (Fig. 4b), as inferred by the cross-like pattern, does not show any lasing threshold. Fluorescence images of the microlasers recorded at the maximum pump power also show a clear difference between the two orientations. In the sideways orientation, two bright spots appear that lie on the opposite sides of the circumference of the microlaser. The anisotropy of the optical texture in the cross-polarized image allows us to identify the direction of the bipolar axis, revealing that these spots are located on the equator of the microsphere. The polar-facing orientation on the other hand only shows homogeneous fluorescence, even at pump energies up to thirty times higher than the threshold energy in the sideways orientation. These experiments, performed by exciting the entire microlaser, indicate that the orientation of the microlasers with respect to the direction of the pump laser plays a crucial role.



**Figure 5:** (a) Cross-polarized image showing multiple bipolar microlasers with different orientations. (b) Emission intensity map obtained by point scanning of the same field of view as in (a) with a confocal hyperspectral microscope at constant pump intensity ( $\sim 400$  pJ). (c) A zoomed-in cross-polarized image (left), intensity map (middle), and spectrum (right) of five selected microlasers (labels corresponding to microlasers in a and b). The first four rows (1-4) show microlasers with a predominantly sideways orientation, each showing two characteristic bright spots on the equatorial plane, while the last microlaser is in a polar-facing orientation and shows almost no detectable emission. The spectra are taken from the pixel with the highest intensity. Scale bar,  $5 \mu\text{m}$ .

To investigate the effect between microlaser orientation and the pumping conditions we changed to a confocal point-scanning microscope and prepared a sample with random orientations of microlasers (Fig. 5a). Here, the field of view is scanned with  $1 \times 1 \mu\text{m}^2$  spatial resolution and with the pulsed pump laser set to a fixed energy (0.4 nJ) that is far above the previously established lasing threshold of microlasers in the sideways orientation. A spectrum is then taken at each point of the image. The resulting intensity map (Fig. 5b) therefore reveals the exact points at which lasing can be excited. First, we observe that roughly half of the microlasers again show exactly two bright spots on their circumference which indicates that they are emitting in the lasing regime (Fig. 4b), while

the other half only shows very weak signals, a clear sign that they are still below the laser threshold. Analyzing optical textures of five selected microlasers (Fig. 5c) reveals that microlasers oriented roughly sideways on their bipolar axis (microlasers 1-4) display the characteristic emission pattern as well as the previously observed split lasing modes. In contrast, microlasers in a polar-facing orientation (microlaser 5) do not display any of the spectral or spatial characteristics associated with lasing. These experiments establish that only microlasers that have a preferential sideways orientation can be excited above the laser threshold and only at two very distinct points on the circumference. This last observation is in strong contrast to our previous experiments where we scanned isotropic polystyrene microlasers which can be excited along their entire circumference and which show an emission pattern where TE and TM modes can be excited preferentially either horizontally or vertically, depending on the alignment of the polarization of the pump laser and the orientation of the WGM.<sup>27,28</sup>

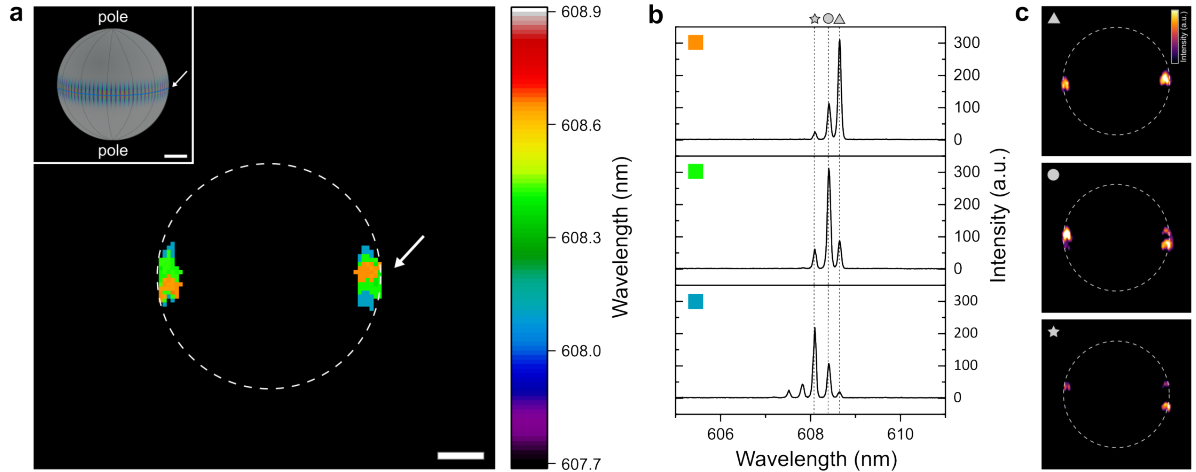


Figure 6: **(a)** High resolution map of the lasing signal of a single sideways-oriented bipolar microlaser obtained by point-scanning with a confocal hyperspectral microscope. For each pixel, the color represents the fitted central wavelength of the laser mode with the highest intensity. Two separate areas are visible, each showing a similar distribution of three distinct wavelengths. The position of the microlaser is represented by a dashed white circle. Inset: Schematic representation of the microlaser orientation. An arrow is pointing at the same position of the equatorial plane in the high resolution map and the schematic representation. Scale bar, 2  $\mu$ m. **(b)** Microlaser spectra calculated by averaging all pixels that have the same color in (a). Vertically dotted lines show that all spectra contain the same 3 modes, representing three sub-modes of a split TE mode which are located at 608.65 nm (triangle), 608.4 nm (circle), and 608.1 nm (star). **(c)** Spectrally separated intensity maps of the three sub-modes visible in (b), showing the intensity distribution of a specific mode in the entire image (symbols corresponding to the mode assignment in (b)). The position of the microlaser is shown by a dashed white circle.

Finally, we investigated the origin of the mode splitting observed in bipolar microlasers by trying to identify the exact spatial position of the different sub-modes. As before we observe lasing at the equatorial plane of a sideways-oriented bipolar microlaser. We then use high-resolution confocal hyperspectral scanning to map the dominant emission wavelength in each pixel (Fig. 6a). Areas, with three distinct lasing wavelengths are observed at the characteristic edge position of the equatorial plane. Plotting the average emission spectra for each of the three colored areas reveals lasing modes at 608.65 nm (orange), 608.4 nm (green), and 608.1 nm (blue), in agreement with previously observed splitting of the TE mode (Fig. 6b, Fig. 3b,d). Notably, all three lasing modes are spatially confined near the equatorial plane, but their spatial position increasingly shifts away from the equator the lower the wavelength of the mode is in the spectrum. Therefore, as the excitation position of the pump laser moves farther away from the equatorial plane, modes with a different wavelength are preferentially excited. In the outermost area, the average spectrum reveals modes with even shorter wavelength though these appear with reduced intensity, while the mode with the longest wavelength vanishes almost completely in this spectrum. Further analyzing the hyperspectral data, we plotted intensity maps of the previously mentioned three wavelengths (Fig. 6c). These maps reveal the spatial mode profile of the corresponding mode in the spectrum. Thus, within a single group of modes, the mode with the longest wavelength is therefore purely confined to the equatorial plane, whereas modes with shorter wavelength are spatially offset towards the bipolar poles and, importantly, show almost no emission at the equatorial plane. These emission patterns are characteristic for higher order azimuthal modes, as we will show in the following.

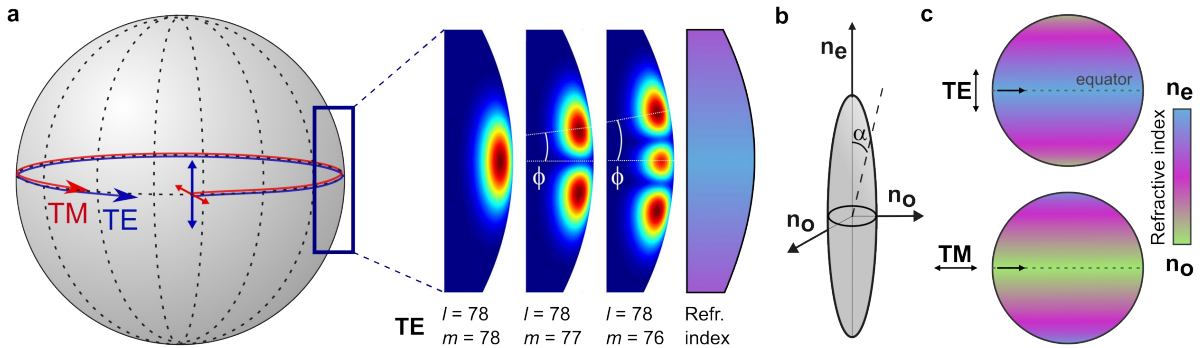


Figure 7: (a) Schematic representation of a bipolar microlaser with arrows showing the propagation and field orientation (i.e. polarization) of TE (blue) and TM (red) modes oscillating in the equatorial plane. The zoomed-in region around the equator shows the cross section of the intensity distribution of three whispering gallery modes (with TE polarizations; TM modes very similar) with the same angular momentum mode number ( $l=78$ ) but different azimuthal mode numbers ( $m=78, 77$ , and  $76$ ). The approximate refractive index distribution in the same area and for a TE mode is shown as well.  $\phi$  is the angle between the equator and the position of the maximum intensity of the mode. Note that  $\phi$  increases with increasing  $m$ , as the mode maximum shifts away from the equator and towards the poles. (b) Sketch of a mesogen with the vectors of the ordinary and extraordinary refractive indices and  $\alpha$  defining the angle between the direction of  $n_e$  and the polarization of the electric field. For the fundamental TE mode ( $m=l$ ), the electric field oscillates parallel to  $n_e$  ( $\alpha=0^\circ$ ), while for TM modes the electric field oscillates perpendicular to  $n_e$  ( $\alpha=90^\circ$ ), i.e. parallel to  $n_o$ . (c) Illustration of the gradient of the refractive index in the entire bipolar microlaser as experienced by TE (top) and TM (bottom) modes, with the direction of propagation shown as an arrow in the sphere. Mode confinement is only efficient for TE modes oscillating in the equatorial plane and with intensity maxima close to the equator.

From the experiments presented so far, we established that molecular self-assembling creates polymer microspheres with a bipolar liquid crystal orientation in which lasing is located only at or close to the equatorial plane. Furthermore, only modes with TE polarization are observed and that these split into groups of modes. From their spatial emission profile and the fact that all modes show similar shifts to external refractive index changes we conclude that only azimuthal WGMs can explain the observed spatial and spectral characteristics.

To further support this conclusion, we calculated mode profiles (TE polarization, angular mode number  $l=78$ , and azimuthal mode number  $m=78, 77$ , and  $76$ ) of the first three azimuthal modes (Fig. 7a). These show that the intensity maxima of azimuthal modes with decreasing mode number  $m$  are shifting from the equator towards the poles, forming an angle  $\phi$  between the equatorial plane and the position of the maximum field intensity.

This is also observed in experimentally determined intensity maps (Fig. 6c). The measured angles are 7.5°, and 12°, while the theoretical values are 7° ( $m = 77$ ), and 11° ( $m = 76$ ). We attribute the difference to the limited resolution in the hyperspectral maps and possible distortions introduced by refraction of the light caused by the difference in refractive index of the microlaser and the surrounding water. Nevertheless, the characteristics of the experimentally observed mode patterns resemble those of the azimuthal mode family.

Regarding the splitting of the modes, we note that azimuthal modes are energetically degenerate in perfectly spherical and isotropic microresonators. However, their degeneracy can be lifted by either deforming the microresonator into an ellipsoid or by introducing an anisotropic refractive index. Here, we argue that the energetic splitting of different azimuthal modes is caused by the refractive index gradient introduced by the bipolar microstructure inside the microlaser. The gradient originates from the gradual variation of the angle  $\alpha$  between the extraordinary refractive index director of the mesogens (aligned planar to the spherical surface, therefore turning with increasing  $\phi$ ) and the polarization of the TE modes (Fig. 7b) which does not, or only gradually, follow the orientation of the mesogens. The gradient can be estimated by using the experimentally determined ordinary and extraordinary refractive index, the WGM mode position obtained from the high-resolution hyperspectral scan (split TE mode with angular mode number  $l = 78$  and lasing peaks at 608.65 nm, 608.4 nm, and 608.1 nm), an external refractive index of 1.333, and the exact (calculated) microlaser size. The effective refractive index profiles for TE and TM modes can be approximated by the following equations (Fig. 7c).

$$n_{TE} = \sqrt{\frac{n_o^2 n_e^2}{n_o^2 \cos^2 \alpha + n_e^2 \sin^2 \alpha}}$$

$$n_{TM} = \sqrt{\frac{n_e^2 n_o^2}{n_e^2 \cos^2 \alpha + n_o^2 \sin^2 \alpha}}$$

From this model we can now see that the purely equatorial lasing of higher-order TE modes arises from the interplay between the propagation direction and polarization of the TE modes (Fig. 7a), and the bipolar alignment of the mesogens within the microlaser. Importantly, due to the perpendicular polarization of TE and TM modes, TE modes experience the extraordinary refractive index, which represents the highest refractive

index in the system, while the TM modes only see the significantly smaller ordinary refractive index (Fig. 7c). Considering also the small size, and the aqueous surrounding medium, efficient confinement is only possible for TE modes at the equatorial plane. For the TE field orientation, the effective refractive index then also decreases towards the bipolar poles causing the observed mode splitting. We can also rule out an alternative explanation for the mode splitting based on the deformation of the microlasers. Achieving an equivalent spectral splitting between adjacent azimuthal modes through geometrical deformation<sup>20</sup> (i.e. from 608.65 nm to 608.4 nm), would require a diameter change of approximately 300 nm. The resulting elliptical deformation, although very small, was not observed in the microlasers.

Despite this overall good agreement between the optical simulations and measurements, variations in the splitting distances between individual modes and between microlasers are observed. These variations are likely caused by a non-uniform mesogen alignment within the microlasers and variations in alignment efficiency from microlaser to microlaser. We assume that these characteristics could be improved by further optimization of the synthetic procedures.

## Conclusion

In summary, we demonstrated the fabrication of highly monodisperse liquid-crystal polymer microlasers with a bipolar internal configuration that supports whispering gallery mode lasing that is restricted to the equatorial plane. These microlasers have low lasing thresholds and are most efficiently excited from the sideview relative to the bipolar axis. In contrast, excitation along the bipolar axis yields only fluorescent emission. Purely equatorial lasing was confirmed by confocal hyperspectral intensity maps correlated with cross-polarized optical images, which reveal both the microlaser orientation and the spatial localization of the lasing emission near the equator.

Furthermore, the microlasers demonstrate pronounced mode splitting which we resolved spatially and spectrally using high-resolution confocal hyperspectral scanning. As the modes shift towards the poles, their effective refractive index decreases, leading to a shorter resonance wavelength. The bipolar liquid crystal configuration induces an internal refractive index gradient that is also experienced differently by modes with the TE or TM polarization. In the small microlasers studied here, the gradient supports lasing only

for TE modes for which the polarization is parallel to the high extraordinary refractive index of the mesogens. A geometrical model links the refractive index gradient to the spatial displacement of the azimuthal modes, which move progressively farther from the equator as the azimuthal mode number decreases. As the spectral splitting depends on the difference between the ordinary and extraordinary refractive index, as well as on the microscopic degree of ordering, analyzing the mode splitting could potentially be used to quantify the order within the liquid crystal phase.

Compared to isotropic spherical microlasers, the strictly confined equatorial lasing in spherical bipolar polymer microlasers might be seen as a potential disadvantage. However, there are several scenarios where this property can be extremely useful. For example, exciting an isotropic microlaser with a scanned focused beam will constantly shift the plane where WGMs oscillate, a consequence from the fact that light incoupling is most efficient at the periphery of the microlaser<sup>27,28</sup>, and that the plane of lasing contains the center of the spherical resonator. If such scanning is performed in a heterogenous environment, e.g. a living cell or small animal, the laser spectra can show significant variations due to refractive index changes in the surrounding of the microlaser<sup>27</sup>. This variation in the resonance positions can then strongly limit the ability for barcoding which is one of the main applications of WGM microlasers. In this context, the additional mode splitting and a more robust read-out might also strongly increase the number of uniquely identifiable tags.

In Additon, we envision that the unique lasing characteristics offers exciting opportunities for highly localized biosensing, where the narrow sensing region can be aligned to a specific structural target inside the biological sample. Finally, the stable mesogen alignment within the spherical microlasers, together with the biocompatibility and elastic properties of the material<sup>36</sup>, may enable future applications in mechanical force sensing<sup>20</sup>. The anisotropic structure of bipolar microlasers likely also leads to an anisotropic elasticity of the polymer matrix<sup>37,38</sup>, However, combined with the geometry-dependent signal generation, the single plane emitting microlasers developed here might even allow to decipher the direction from where the force acts on the microlaser.

## **Methodes**

**Materials and Chemicals.** Monodisperse microlasers were fabricated with commercial focused flow droplet generator microfluidic chips (20  $\mu\text{m}$  nozzle, 11002137, Micronit). The monomer 4-methoxybenzoic acid 4-(6-acryloyloxy-hexyloxy)phenyl ester (CAS: 130953-14-9, ST03866, SYNTHON Chemicals) and the crosslinker 1,4-Bis[4-(3-acryloyloxypropoxy) benzoyloxy]-2-methylbenzene (CAS: 174063-87-7, ST03021, SYNTHON Chemicals) and the initiator 2-Benzyl-2-(dimethylamino)-4'morpholinobutyrophenone (Irgacure<sup>®</sup> 369, Tokyo Chemical Industry) were used as received. For planar anchoring poly(vinyl alcohol) (PVA,  $n = \text{approx. } 2000$ , degree of saponification ca. 80mol%, Tokyo Chemical Industry) was used. As gain medium 4-(Dicyanomethylene)-2-methyl-6-(4-dimethylaminostyryl)-4H-pyran (DCM, CAS: 51325-91-8, Sigma Aldrich) was used and solutions were made with dichloromethane ( $\text{CH}_2\text{Cl}_2$ ) and toluene (Sigma Aldrich). All solutions were filtered by 0.22  $\mu\text{m}$  PTFE filters (514-1275, VWR).

**Microlaser preparation.** Highly monodisperse dye-doped liquid crystal polymer microspheres were prepared by microfluidics. For the dispersed phase a mixture of monomer (50 mg), crosslinker (8.4 mg, 10 mol%), initiator (1 mg, 2 mol%) and lasing-dye (2 wt%, in relation to the total mass of the liquid crystal polymer mix) were dissolved in 1.2 ml of dichloromethane. For the continuous phase, a 0.2% w/v aqueous PVA solution was prepared. Before using the prepared solutions for microfluidics, they were filtered by 0.22  $\mu\text{m}$  PTFE filters. A 20  $\mu\text{m}$  nozzle focused flow droplet generator chip was used, and pressure was applied by a custom build pressure system to control the flow of the two phases. The droplet size could be tuned between 25 and 30  $\mu\text{m}$ . The collected droplets were shaken at 900 rpm for 2 h for the dichloromethane to evaporate. The resulting liquid crystal droplets had a monodisperse size between 9 and 10  $\mu\text{m}$ . In a next step, the droplets were polymerized under continuous rotational movement by exposing them to UV light (366 nm) for 20 min. The crosslinked liquid crystal polymer microspheres were separated from the surfactant solution by centrifugation and washed once with DI water. For storage the microspheres were re-dispersed in a 0.05% w/v aqueous PVA solution.

**Refractive index measurement by ellipsometry.** The refractive index was determined by variable angle spectroscopic ellipsometry (M2000, J.A. Woollam), modeled with a biaxial anisotropic oscillator model (CompleteEASE, J.A. Woollam). Measurements of an

aligned and isotropic thin films of the liquid crystal polymer were performed. For the aligned film, a silicon wafer was cleaned with acetone and isopropanol for 15 min in an ultrasonic bath each and spin coated with a 0.05% w/v PVA solution (3000 rpm, 1000 rpm/s, 60 s). The PVA film was rubbed manually unidirectional with wipes (115-1803, VWR) and cleaned with toluene for 3 min in an ultrasonic bath. The same liquid crystal monomer, crosslinker, and initiator mix used for the microlaser preparation (but without the lasing dye) was dissolved in toluene with a concentration of 9% w/v. The dissolved mix was spin coated on the PVA film (900 rpm, 450 rpm/s, 30 s) and photopolymerized under UV light at room temperature for 20 min, achieving an aligned 600 nm thick liquid crystal polymer film. The film was characterized by ellipsometry to determine the ordinary and extraordinary refractive index. For the isotropic film the liquid crystal polymer mix was directly spin coated on the silicon wafer without the PVA alignment film and polymerized for 20 min at 80 °C under UV light.

**Optical characterization.** Lasing threshold measurements, refractive index sensing and cross-polarized imaging were performed on a standard inverted fluorescence microscope (TE2000, Nikon). For the lasing experiments a green short-pulsed diode-pumped solid-state laser (515 nm, Flare NX 515-0.6-2, COHERENT), running at a repetition rate of 100 Hz with a pulse length of 1.15 ns, is coupled by a dichroic mirror into the microscope and directed on to the sample by a microscope objective (extra-long working distance (ELWD) 40x, numerical aperture (NA) 0.60, Nikon). Here, entire microlasers are pumped with the green pump laser. The emission from the microlasers is collected by the same objective and directed to a spectrograph (Iso-plane SCT320, Princeton Instruments) equipped with a 1200 lines per mm grating and a CCD camera (Blaze 400HR, Princeton Instruments) and a spectral resolution of about 50 pm. Simultaneously, differential interference contrast (DIC) imaging or cross-polarized imaging can be conducted by using the transmission light pass of the microscope and by directing the transmitted light from the sample to a sCMOS camera (ORCA-Flash4.0 V3 C13440-20CU, Hamamatsu) using a dichroic mirror. For cross-polarized imaging, a polarizer is placed between sample and dia-illumination, and a second polarizer (analyser) is placed perpendicular to the polarization of the first polarizer between sample and camera. Threshold measurements were performed with microlasers stabilized in a 0.25% w/v agarose matrix to avoid movement during the measurement. To

change the pump energy, a set of optical density filter with different optical densities was inserted into the excitation light path before being coupled to the microscope. Refractive index sensing was carried out with microlasers in water and consecutively adding a 30% w/v glucose solution to increase the refractive index.

**Confocal Hyperspectral imaging.** Two different setups were used for confocal hyperspectral imaging. The first setup was used to scan a large field of view with multiple microlasers and simultaneous cross-polarized imaging (Fig. 5). The liquid crystal polymer microlasers were fixed in a 0.25% w/v agarose matrix and imaged on a hyperspectral laser scanning confocal microscope. The setup was built around a standard inverted fluorescence microscope (TE2000, Nikon). A 515 nm pulsed laser (Origami-05XP, NKT Photonics) with a pulse width of 370 fs and a pulse repetition rate of 100 kHz was used as the pump source. The pulse energy was coarsely adjusted within the laser head, and a half-wave plate in combination with a polarizing beam splitter was used for fine control. The collimated laser beam was expanded and focused on the sample through a microscope objective (ELWD 40x, NA 0.60, Nikon). The pulse energy at the image plane was measured to be approximately 400 pJ. Fast galvo mirrors (5 mm aperture, Saturn 5B, ScannerMAX) were used to scan the beam across a 210 x 210  $\mu\text{m}$  scan-field with a spatial resolution of 1 pixel/ $\mu\text{m}^2$ . The pixel dwell time was 1000  $\mu\text{s}$ , consisting of 100  $\mu\text{s}$  exposure and 900  $\mu\text{s}$  spectrometer readout. The signal from the microlasers was collected through the same objective and de-scanned. A dichroic beam splitter and a focusing lens was used to direct the de-scanned signal to the entrance slit of the spectrograph (see above). The spectral CCD camera readout was limited to the top 50 lines in vertical binning mode to increase a spectral read-out rate of 1 kHz. The slit of the spectrometer served as a confocal pinhole and improved the spectral and spatial resolution. A full image in this operation mode was captured in 44.1 seconds. The galvos and the spectrometer, microscope stage, and the fine laser power control were synchronized using a custom-built LabVIEW script. The pump laser was triggered by the spectrometer CCD to emit only during the exposure. In the acquired hyperspectral data set, each of the 44100 pixels in the scan-field contains a high-resolution spectrum which is analyzed by a custom python script to perform a Voigt fit on all lasing peaks to extract the peak wavelength, intensity, and widths. DIC and cross-polarized images of the same field of view were captured

sequentially as described above to allow comparison of the microlaser orientation and axis of lasing.

The second hyperspectral microscope was used for high resolution scanning of a single microlaser (Fig. 6) by using a commercial laser scanning microscope (Stellaris 8, Leica), which we described in detail in a recent publication.<sup>28</sup> Here, a spatial (pixel) resolution of 190 nm and spectral resolution of 50 pm was achieved.

**Mode calculation and visualization.** Calculated resonances for the fundamental ( $m=l$ ) angular momentum whispering gallery modes were obtained using a custom code and the model proposed by Schiller<sup>35</sup> also used in a previous publication<sup>3</sup>, while for azimuthal modes the model by Gorodetsky<sup>39</sup> and Demchenko<sup>40</sup> was used, also applied in a recent publication<sup>20</sup>. All mode visualizations were performed in MATLAB using a previously published toolbox by that was further modified and extended for this work.<sup>41</sup>

**Refractive index gradient calculation.** To calculate the effective refractive index of a liquid crystal, related to the angle between the extraordinary or ordinary refractive index and the light field orientation, the standard equation for an ellipse centered at (0, 0) is used.

$$\frac{y^2}{a^2} + \frac{x^2}{b^2} = 1 \text{ (for } a > b\text{)}$$

By trigonometric functions and replacing  $a$  by the extraordinary refractive index and  $b$  by the ordinary refractive index, we receive an equation to determine the effective refractive index.

## Funding

This work received instrument funding by the Deutsche Forschungsgemeinschaft in cooperation with the Ministerium für Kunst und Wissenschaft of North Rhine-Westphalia (INST 216/1120-1 FUGG, 469988234), and research funding from the European Research Council under the European Union’s Horizon Europe Framework Program (ERC Starting Grant agreement no. 101043047 (HYPERION, to M.S.)).

## Data availability

Data underlying the results presented in this paper are not publicly available at this time but can be obtained from the authors.

## Disclosures

The authors declare no conflicts of interest.

## References

- (1) Thomson, C. A.; Popczyk, A.; Schubert, M.; Gather, M. C. Biointegrated Microlasers: Technologies, Applications, and Emerging Developments. *Optica* 2025, 12 (8), 1311. <https://doi.org/10.1364/optica.563263>.
- (2) Schubert, M.; Woolfson, L.; Barnard, I. R. M.; Dorward, A. M.; Casement, B.; Morton, A.; Robertson, G. B.; Appleton, P. L.; Miles, G. B.; Tucker, C. S.; Pitt, S. J.; Gather, M. C. Monitoring Contractility in Cardiac Tissue with Cellular Resolution Using Biointegrated Microlasers. *Nat. Photonics* 2020, 14 (7), 452–458. <https://doi.org/10.1038/s41566-020-0631-z>.
- (3) Fikouras, A. H.; Schubert, M.; Karl, M.; Kumar, J. D.; Powis, S. J.; Di Falco, A.; Gather, M. C. Non-Obstructive Intracellular Nanolasers. *Nat. Commun.* 2018, 9 (1), 4817. <https://doi.org/10.1038/s41467-018-07248-0>.
- (4) Humar, M.; Hyun Yun, S. Intracellular Microlasers. *Nat. Photonics* 2015, 9 (9), 572–576. <https://doi.org/10.1038/nphoton.2015.129>.
- (5) Schubert, M.; Volckaert, K.; Karl, M.; Morton, A.; Liehm, P.; Miles, G. B.; Powis, S. J.; Gather, M. C. Lasing in Live Mitotic and Non-Phagocytic Cells by Efficient Delivery of Microresonators. *Sci. Rep.* 2017, 7 (1), 40877. <https://doi.org/10.1038/srep40877>.
- (6) Titze, V. M.; Caixeiro, S.; Di Falco, A.; Schubert, M.; Gather, M. C. Red-Shifted Excitation and Two-Photon Pumping of Biointegrated GaInP/AlGaInP Quantum Well Microlasers. *ACS Photonics* 2022, 9 (3), 952–960. <https://doi.org/10.1021/acsphotonics.1c01807>.
- (7) Caixeiro, S.; Kunstmann-Olsen, C.; Schubert, M.; Hill, J.; Barnard, I. R. M.; Simmons, M. D.; Johnson, S.; Gather, M. C. Local Sensing of Absolute Refractive Index During Protein-Binding Using Microlasers with Spectral Encoding. *Adv. Opt. Mater.* 2023, 2300530. <https://doi.org/10.1002/adom.202300530>.

(8) Caixeiro, S.; Dörrenhaus, R.; Popczyk, A.; Schubert, M.; Kath-Schorr, S.; Gather, M. C. DNA Sensing with Whispering Gallery Mode Microlasers. *Nano Lett.* 2025, 25 (11), 4467–4475. <https://doi.org/10.1021/acs.nanolett.5c00078>.

(9) Schubert, M.; Steude, A.; Liehm, P.; Kronenberg, N. M.; Karl, M.; Campbell, E. C.; Powis, S. J.; Gather, M. C. Lasing within Live Cells Containing Intracellular Optical Microresonators for Barcode-Type Cell Tagging and Tracking. *Nano Lett.* 2015, 15 (8), 5647–5652. <https://doi.org/10.1021/acs.nanolett.5b02491>.

(10) Martino, N.; Kwok, S. J. J.; Liapis, A. C.; Forward, S.; Jang, H.; Kim, H. M.; Wu, S. J.; Wu, J.; Dannenberg, P. H.; Jang, S. J.; Lee, Y. H.; Yun, S. H. Wavelength-Encoded Laser Particles for Massively Multiplexed Cell Tagging. *Nat. Photonics* 2019, 13 (10), 720–727. <https://doi.org/10.1038/s41566-019-0489-0>.

(11) Wang, Y.; Li, H.; Zhao, L.; Liu, Y.; Liu, S.; Yang, J. Tunable Whispering Gallery Modes Lasing in Dye-Doped Cholesteric Liquid Crystal Microdroplets. *Appl. Phys. Lett.* 2016, 109 (23), 231906. <https://doi.org/10.1063/1.4971973>.

(12) Zhao, L.; Wang, Y.; Yuan, Y.; Liu, Y.; Liu, S.; Sun, W.; Yang, J.; Li, H. Whispering Gallery Mode Laser Based on Cholesteric Liquid Crystal Microdroplets as Temperature Sensor. *Opt. Commun.* 2017, 402, 181–185. <https://doi.org/10.1016/j.optcom.2017.06.008>.

(13) Pirnat, G.; Humar, M.; Muševič, I. Remote and Autonomous Temperature Measurement Based on 3D Liquid Crystal Microlasers. *Opt. Express* 2018, 26 (18), 22615. <https://doi.org/10.1364/oe.26.022615>.

(14) Lee, S. S.; Kim, J. Bin; Kim, Y. H.; Kim, S.-H. Wavelength-Tunable and Shape-Reconfigurable Photonic Capsule Resonators Containing Cholesteric Liquid Crystals. *Sci. Adv.* 2018, 4 (6), 1–9. <https://doi.org/10.1126/sciadv.aat8276>.

(15) Franklin, D.; Ueltschi, T.; Carlini, A.; Yao, S.; Reeder, J.; Richards, B.; Van Duyne, R. P.; Rogers, J. A. Bioresorbable Microdroplet Lasers as Injectable Systems for Transient Thermal Sensing and Modulation. *ACS Nano* 2021, 15 (2), 2327–2339. <https://doi.org/10.1021/acs.nano.0c10234>.

(16) Humar, M.; Ravnik, M.; Pajk, S.; Muševič, I. Electrically Tunable Liquid Crystal Optical Microresonators. *Nat. Photonics* 2009, 3 (10), 595–600. <https://doi.org/10.1038/nphoton.2009.170>.

(17) Sofi, J. A.; Mohiddon, M. A.; Dutta, N.; Dhara, S. Electrical and Thermal Tuning of Quality Factor and Free Spectral Range of Optical Resonance of Nematic Liquid Crystal Microdroplets. *Phys. Rev. E* 2017, 96 (2), 022702. <https://doi.org/10.1103/PhysRevE.96.022702>.

(18) Sofi, J. A.; Dhara, S. Electrically Switchable Whispering Gallery Mode Lasing from Ferroelectric Liquid Crystal Microdroplets. *Appl. Phys. Lett.* 2019, 114 (9). <https://doi.org/10.1063/1.5088863>.

(19) Dalaka, E.; Hill, J. S.; Booth, J. H. H.; Popczyk, A.; Pulver, S. R.; Gather, M. C.; Schubert, M. Deformable Microlaser Force Sensing. *Light Sci. Appl.* 2024, 13 (1). <https://doi.org/10.1038/s41377-024-01471-9>.

(20) Pirnat, G.; Marinčič, M.; Ravnik, M.; Humar, M. Quantifying Local Stiffness and Forces in Soft Biological Tissues Using Droplet Optical Microcavities. 2024. <https://doi.org/10.1073/pnas>.

(21) Duan, R.; Li, Y.; Shi, B.; Li, H.; Yang, J. Real-Time, Quantitative and Sensitive Detection of Urea by Whispering Gallery Mode Lasing in Liquid Crystal Microdroplet. *Talanta* 2020, 209. <https://doi.org/10.1016/j.talanta.2019.120513>.

(22) Nie, N.; Gong, X.; Gong, C.; Qiao, Z.; Wang, Z.; Fang, G.; Chen, Y. C. A Wearable Thin-Film Hydrogel Laser for Functional Sensing on Skin. *Anal. Chem.* 2024, 96 (22), 9159–9166. <https://doi.org/10.1021/acs.analchem.4c00979>.

(23) Duan, R.; Hao, X.; Li, Y.; Li, H. Detection of Acetylcholinesterase and Its Inhibitors by Liquid Crystal Biosensor Based on Whispering Gallery Mode. *Sens. Actuators B Chem.* 2020, 308 (November 2019), 127672. <https://doi.org/10.1016/j.snb.2020.127672>.

(24) Duan, R.; Li, Y.; Li, H.; Yang, J. Detection of Heavy Metal Ions Using Whispering Gallery Mode Lasing in Functionalized Liquid Crystal Microdroplets. *Biomed. Opt. Express* 2019, 10 (12), 6073. <https://doi.org/10.1364/BOE.10.006073>.

(25) Humar, M.; Muševič, I. Surfactant Sensing Based on Whispering-Gallery-Mode Lasing in Liquid-Crystal Microdroplets. *Opt. Express* 2011, 19 (21), 19836. <https://doi.org/10.1364/OE.19.019836>.

(26) Yamamoto, Y. Spherical Resonators from  $\pi$ -Conjugated Polymers. *Polymer Journal*. Nature Publishing Group November 1, 2016, pp 1045–1050. <https://doi.org/10.1038/pj.2016.81>.

(27) Oki, O.; Kulkarni, C.; Yamagishi, H.; Meskers, S. C. J.; Lin, Z. H.; Huang, J. S.; Meijer, E. W.; Yamamoto, Y. Robust Angular Anisotropy of Circularly Polarized Luminescence from a Single Twisted-Bipolar Polymeric Microsphere. *J. Am. Chem. Soc.* 2021, 143 (23), 8772–8779. <https://doi.org/10.1021/jacs.1c03185>.

(28) Cowie, R. C.; Schubert, M. Light Sheet Microscope Scanning of Biointegrated Microlasers for Localized Refractive Index Sensing. *Photonics Res.* 2024, 12 (8), 1673. <https://doi.org/10.1364/prj.522018>.

(29) Titze, V. M.; Caixeiro, S.; Dinh, V. S.; König, M.; Rübsam, M.; Pathak, N.; Schumacher, A. L.; Germer, M.; Kukat, C.; Niessen, C. M.; Schubert, M.; Gather, M. C. Hyperspectral Confocal Imaging for High-Throughput Readout and Analysis of Bio-Integrated Microlasers. *Nat. Protoc.* 2024, 19 (3), 928–959. <https://doi.org/10.1038/s41596-023-00924-6>.

(30) Ferrantini, C.; Pioner, J. M.; Martella, D.; Coppini, R.; Piroddi, N.; Paoli, P.; Calamai, M.; Pavone, F. S.; Wiersma, D. S.; Tesi, C.; Cerbai, E.; Poggesi, C.; Sacconi, L.; Parmeggiani, C. Development of Light-Responsive Liquid Crystalline Elastomers to Assist Cardiac Contraction. *Circ. Res.* 2019, 124 (8), e44–e54. <https://doi.org/10.1161/CIRCRESAHA.118.313889>.

(31) Schiller, S. *Asymptotic Expansion of Morphological Resonance Frequencies in Mie Scattering*; 1993.

(32) Gorodetsky, M. L.; Fomin, A. E. Geometrical Theory of Whispering-Gallery Modes. *IEEE Journal on Selected Topics in Quantum Electronics* 2006, 12 (1), 33–39. <https://doi.org/10.1109/JSTQE.2005.862954>.

(33) Demchenko, Y. A.; Gorodetsky, M. L. Analytical Estimates of Eigenfrequencies, Dispersion, and Field Distribution in Whispering Gallery Resonators. *Journal of the*

*Optical Society of America* B 2013, 30 (11), 3056.

<https://doi.org/10.1364/josab.30.003056>.

(34) Balac, S. WGMode: A Matlab Toolbox for Whispering Gallery Modes Volume Computation in Spherical Optical Micro-Resonators. *Comput. Phys. Commun.* 2019, 243, 121–134. <https://doi.org/10.1016/j.cpc.2019.05.002>.